FULL PAPER

Polar Cation Ordering: A Route to Introducing >10% Bond Strain Into Layered Oxide Films

*Brittany B. Nelson-Cheeseman, Hua Zhou, Prasanna V. Balachandran, Gilberto Fabbris, Jason Hoffman, Daniel Haskel, James M. Rondinelli, and Anand Bhattacharya**

The 3*d* transition metal (*M*) perovskite oxides exhibit a remarkable array of properties, including novel forms of superconductivity, magnetism and multiferroicity. Strain can have a profound effect on many of these properties. This is due to the localized nature of the M 3*d* orbitals, where even small changes in the *M*–O bond lengths and *M*–O–M bond angles produced by strain can be used to tune the 3*d*– O 2*p* hybridization, creating large changes in electronic structure. A new route is presented to strain the M–O bonds in epitaxial two-dimensional perovskite films by tailoring local electrostatic dipolar interactions within every formula unit via atomic layer-by-layer synthesis. The response of the O anions to the resulting dipole electric fields distorts the *M*–O bonds by more than 10%, without changing substrate strain or chemical composition. This distortion is largest for the apical oxygen atoms (O_{ap}), and alters the transition metal valence state via self-doping without chemical substitution.

1. Introduction

Varying elastic strain is a powerful method for realizing new and enhanced properties of materials. This approach is particularly effective in the transition metal oxides (TMOs), where small changes in the transition metal-oxygen bond lengths and bond angles can transform electronic structure[1] and properties,[2–5] due to changes in transition metal-oxygen hybridization. In thin films of TMOs, epitaxial strain values between -2.4% (compressive) to 1.1% (tensile) have been successfully used to control a wide range of properties, including ferroelectricity,[6] magnetism,[7] and multiferroicity.[8] However, there are limitations to this approach. Firstly, this technique only allows for direct control of in-plane strain, while bonds in the out-of-plane direction change according to the Poisson effect. Moreover, strain values of more than ≈2–3% are not possible to sustain in epitaxial films that are thicker than a few layers, as they rapidly relax back to their bulk structure via misfit dislocations. Attaining larger bond strains in this class of materials would likely uncover new and enhanced properties. Indeed, large local bond strain arising at surfaces[9] or at the interface between two materials has been documented in the literature,[10] and has been related to intriguing interfacial states.[11] However, the community has yet to devise a strategy to impose large (>5%) bond strains throughout a single phase TMO material.

Here, we demonstrate a new paradigm for creating bond strains via polar distortions that arise due to electrostatic forces throughout a thin film of a model layered perovskite, $LaSrNiO_4$ (LSNO), a paramagnetic metal. Similar to how "epitaxial strain" or "chemical strain"[12] are used to indicate elastic bond strain resulting from an imposed "epitaxial stress" or "chemical stress", respectively, here we define the term "electrostatic bond strain" to denote changes in bond length (strain) that result from introducing additional dipolar electrostatic fields via polar cation ordering (the term "electrostatic strain" has also been used in the context of biological molecules).[13] This method allows us to strain the Ni-O_{ap} bond (along the c-axis) by an amount far in excess of what can be accomplished via applying epitaxial strain in the *a*–*b* plane and relying on the Poisson ratio. Our approach is not limited by the thickness of the film.

Prof. B. B. Nelson-Cheeseman, Dr. J. Hoffman, Dr. A. Bhattacharya
Materials Science Division
Argonne National Lab
Argonne, IL 60439, USA
E-mail: anand@anl.gov
Prof. B. B. Nelson-Cheeseman
School of Engineering
University of St. Thomas
St. Paul, MN 55105, USA
Dr. H. Zhou, G. Fabbris, Dr. D. Haskel
Advanced Photon Source
Argonne National Lab
Argonne, IL 60439, USA
Dr. P. V. Balachandran, Prof. J. M. Rondinelli[+]
Dept of Materials Science and Engineering
Drexel University
Philadelphia, PA 19104, USA
G. Fabbris
Department of Physics
Washington University
St. Louis, MO 60130, USA
Dr. A. Bhattacharya
Center for Nanoscale Materials
Argonne National Lab
Argonne, IL 60439, USA
[+]Present address: Department of Materials Science and Engineering
Northwestern University, Evanston, IL 60208, USA

DOI: 10.1002/adfm.201401077

Using ozone-assisted molecular beam epitaxy (MBE), we create polar analogs of $LaSrNiO_4$, where the cations are arranged in fully ordered (001) layers in a manner that breaks inversion symmetry. Specifically, the crystal is constructed from positively charged $[LaO]^{(1+)}$, neutral $[SrO]^{(0)}$, and negatively charged $[NiO_2]^{(1-)}$ planes, yielding Ni cations of nominal 3+ oxidation state in every formula unit (f.u.). Varying the sequence of the charged layers can be used to tailor local electrostatic forces within a single f.u., providing a powerful pathway to direct distortions of the Ni-O bonds, moving the Ni off center within the NiO_6 octahedral cage. This enables control over the Ni electronic state at fixed $LaSrNiO_4$ composition, via changes in Ni-O hybridization. We determine the positions of all atoms in the films with sub-Å resolution by measuring X-ray crystal truncation rods and using a phase retrieval technique known as COBRA (COherent Bragg Rod Analysis).[14] We find that the NiO_6 octahedra distort to produce Ni-apical oxygen ($Ni\text{-}O_{ap}$) bond length changes as large as 15% in the polar $LaSrNiO_4$ variant compared to those in centrosymmetric solid-solution structures. We then measure the response of the electronic structure to these distortions via X-ray absorption spectroscopy (XAS) at the Ni *K*-edge. Finally, we disentangle the effects of Ni-O bond distortions on the electronic state via ab initio band structure calculations. Our study reveals that control over dipolar interactions by means of chemical ordering provides a route to control *M*–O bonds and thereby to direct orbital filling, which is essential for stabilizing novel electronic and magnetic states in these layered materials with correlated electrons.

2. Results and Discussion

We synthesized epitaxial two-dimensional (2D) Ruddlesden-Popper (RP) (single layer) films of $LaSrNiO_4$ by oxide-MBE on isostructural (001)-oriented $LaSrAlO_4$ (LSAO) single crystal substrates. Within a single f.u. of $LaSrNiO_4$, we permuted the LaO and SrO layers to obtain several chemically equivalent structures with different electrostatic configurations. In the present work, we focus on the following layering sequences for *n* unit cells (u.c.), each consisting of two formula units (**Figure 1**):

i. Alloy: $[(La_{0.5}Sr_{0.5})O/NiO_2/(La_{0.5}Sr_{0.5})O]\times 2n$,

ii. LNS/LNS: $[\{LaO/NiO_2/SrO\}/\{LaO/NiO2/SrO\}]\times n$, and

iii. SNL/SNL: $[\{SrO/NiO_2/LaO\}/\{SrO/NiO2/LaO\}]\times n$.

We note that structural variants ii) "LNS/LNS" and iii) "SNL/SNL" are related by a mirror symmetry element and are obtained by reversing the layer-by-layer growth sequence. Both variants lack inversion symmetry, yielding polar (along *c*-axis) structures, while the alloy is centrosymmetric.[15] The thickness of films chosen here was dictated by the limitations of COBRA analysis, which works best for films that are less than ≈6–8 nm thick. Thicker films (up to 30 f.u.) grown in the same manner had comparable surface crystallinity and smoothness during growth, as measured with RHEED (reflection high energy diffraction), and bulk structure, as measured by x-ray reflectivity and diffraction.[16]

In order to impose electrostatic bond strain on the Ni–O bonds throughout the $LaSrNiO_4$ film, we need to realize dipolar electrostatic fields within every formula unit, without altering the composition. There are two aspects of the $AA'MO_4$ RP perovskite structure that enable us to realize this. Firstly, each formula unit is composed of three layers ($AO\text{-}MO_2\text{-}A'O$) along the [001] direction that allows for asymmetric tuning of the *M* environment within a given f.u. by choosing different *A* and *A'* atoms, as discussed in the previous paragraph. This is not feasible in the AMO_3 perovskites, which are composed of only two layers ($AO\text{-}MO_2$) along [001]. Secondly, the $Ni\text{–}O_{ap}$ bonds are not as constrained in the $AA'MO_4$ structure since the MO_6 octahedra are not connected to each other along [001]. This allows the $Ni\text{–}O_{ap}$ bond to undergo large distortions in response to electrostatic forces. However, realizing cation-ordered RP structures[17,18] is challenging due to intermixing between the *AO* and *A'O* layers that are immediately adjacent to each other in a rocksalt block, as in $AO\text{-}A'O\text{-}MO_2\text{-}AO\text{-}A'O\text{-}MO_2$. Small differences in *A*-site cation valence (e.g., A^{2+}, A'^{3+}) and ionic size favor intermixing as a means to minimize electrostatic and steric forces.[19] We note that *A*-site cation ordering is easier to achieve in $AMO_3/A'MO_3$ superlattices of 3D perovskite oxides,[20–27] where the layer sequence is $AO\text{-}MO_2\text{-}A'O\text{-}MO_2$, and *A*/*A'* intermixing requires exchange through an MO_2 barrier layer.[28] Nevertheless, we are able to realize cation ordering in the RP $LaSrNiO_4$ structure (see Figure S1, Supporting Information, for evidence of cation ordering within a rocksalt block) by digitally interleaving layers of LaO, SrO and NiO_2 during growth (see Experimental Section). Solid solution LSNO films, where the La and Sr cations are completely mixed, are obtained by co-depositing La and Sr in $(La_{0.5}Sr_{0.5})O$ layers followed by the NiO_2 layers (Alloy variant). Tricolor superlattices

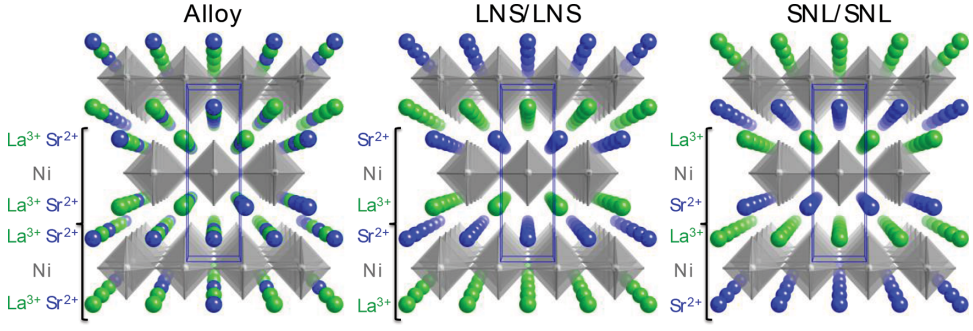

Figure 1. Digital A-site layering sequences for La (Green) and Sr (Blue) within one $LaSrNiO_4$ unit cell. Left to right: Alloy, LNS/LNS, SNL/SNL. Note charged (+) and neutral (0) A-site layers from $[LaO]^{(1+)}$ and $[SrO]^{(0)}$, respectively.

comprising integer unit cells of three different components have been used to create structures with broken inversion symmetry in other materials.[24–26] However, in our work we show that as long as a crystal has a unit cell defined by interleaved metal-oxide layers and cations of different valence, it may be possible to realize a polar analog of the material by rearranging the cations within a single unit cell, without altering the overall chemical composition.

To determine the cation order and the Ni-O bond lengths and bond angles in our samples, we measure specular and off-specular crystal truncation rods (CTRs) by surface X-ray diffraction (see the Experimental Section). We combine this with COBRA,[14] an X-ray direct method that applies an iterative process of alternatively satisfying constraints in real and reciprocal space to reconstruct the diffraction phases from measured diffraction intensities (see Supporting Information for more about COBRA data analysis). This enables us to determine the full atomic structure within each f.u. of the ultrathin films grown on LSAO substrates,[10] including all cation and oxygen positions.[29] This is carried out for all LSNO cation layering variants, revealing local structural information that is otherwise inaccessible via standard X-ray analysis.

The COBRA-determined 2D electron density (ED) maps [i.e., (100) and (200) atomic planes] for the three layering sequences reveal the atomic arrangement inside the films (**Figure 2**a–c, upper panels). Since the La and Sr at the *A*-site have different integrated electron densities (i.e., 57 and 35, respectively),[30] the relative electron density (brightness) in the *A*-site positions is indicative of the degree of cation ordering/mixing. We find evidence of the mixed *vs.* ordered La/Sr *A*-site occupations in the Alloy versus LNS/LNS and SNL/SNL films in the ED profiles. We quantify the degree of ordering by examining the integrated electron number of *A*-site cations obtained from the ED profile as a function of position (Figure 2a–c, lower panels), and comparing it to the nominal growth sequence. The Alloy film shows a mixed *A*-site occupation, with ≈50% Sr/50% La per site. In contrast, the cation-ordered LNS/LNS film exhibits alternating La and Sr *A*-site occupation. [This effect is reproduced in a second LNS/LNS sample, from a different growth (Figure S3, Supporting Information).] From the contrast, we estimate 96 (± 3.9)% cation ordering in this variant (see Supporting Information for error bar estimation), that is, the "La" sites have only a small fraction of Sr intermixed and vice versa. Upon reversing the growth sequence to SNL/SNL, we measure a reversed alternating occupation on the *A*-site by Sr and La, as expected, but with reduced ED variation. We estimate that the degree of cation ordering in this sample is lower, with the Sr sites being occupied by 75 (± 3.9)% Sr/25 (±3.5)% La, and vice-versa. While we do not have a clear explanation for the intermixing in the SNL/SNL sample, we note that in alloy samples of the single layer cuprate $La_{1.56}Sr_{0.44}CuO_4$, the $La_{1-x}Sr_xO$ layer directly above the CuO_2 layer (in the growth direction) has been shown to be more Sr-rich compared to the one below.[31] Thus, SrO may have a preferred position with respect to the NiO_2 plane. A detailed study of cation intermixing in different cation ordered variants of $LaSrNiO_4$ is currently underway.[16] We also observe a significant reduction of the integrated electron number near the surface of the film, regardless of cation ordering, as is often the case in surface X-ray diffraction measurements.[29] This is

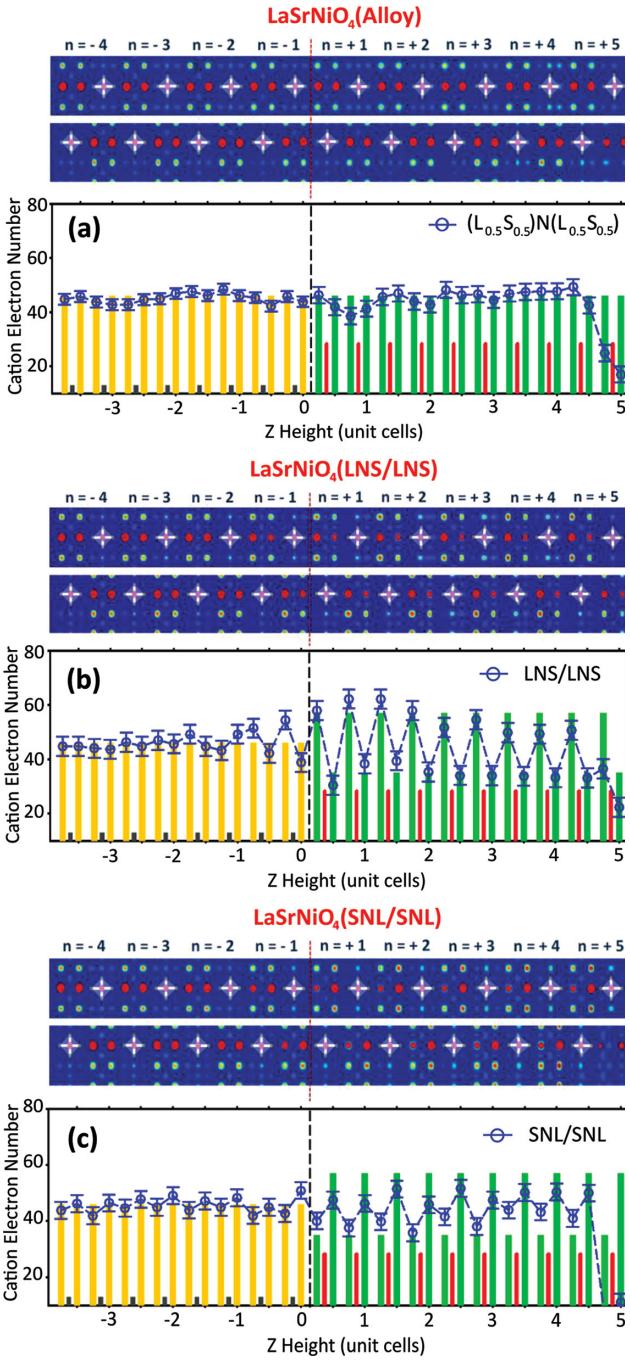

Figure 2. COBRA-determined electron density of Alloy, LNS/LNS and SNL/SNL films thru film thicknesses. Upper panels in (a–c): 2D ED profiles along (100) and (200) atomic planes. Cold colors represent low ED, while warmer colors represent higher ED. The projected shapes of the NiO_6/(AlO_6) octahedra are highlighted by the schematic drawings. Note that due to the layered perovskite structure, the Ni octahedra are visible in only every other nickelate layer for a given (h00) plane. Lower panels in (a–c): The integrated electron number of A-site cations obtained from ED profile as a function of *Z* height. The alternating La/Sr occupations on the A-site across the film illustrate directly the LNS/LNS and SNL/SNL cation ordering. The nominal A-site cation distributions for each variant are marked with orange (substrate side) and green bars (film side), respectively. The grey and red bars signify the positions of alumina and nickelate layers, respectively. The red bars indicate the position of the Ni cations within the film.

understood to be a result of incomplete surface layer occupation (see also Supporting Information).[32]

We now investigate how the NiO_6 environment responds to the charged *AO* plane sequence in the LSNO variants. We find that both the Ni–O_{ap} and Ni–O_{eq} (Ni-equatorial oxygen) bonds react strongly to the *AO* layering in the polar LSNO variants. **Figure 3**a–c depicts the Ni-O_{ap} bond length evolution as a function of *Z* height within the film for the three sample types. For the LNS/LNS sample in Figure 3b, the two inequivalent apical oxygens in the LaO and in the SrO layers behave differently with increasing film thickness. The Ni-O_{ap} bond to the O in the SrO layer contracts, while the Ni–O_{ap} bond to the O in the LaO layer elongates. The effect is, on average, larger near the film/surface interface than near the film/substrate interface. [Investigations of a different LNS/LNS sample show a similar trend (Figure S3, Supporting Information).] In order to minimize anomalous sources of error (such as surface or substrate-film interface effects), we measured the reversed SNL/SNL sample, and also an Alloy sample where the polar cation order is absent. Figure 3c shows that the charge layer sequence reversal (SNL/SNL) results in a reversal of the Ni–O_{ap} bond distortions as well, demonstrating that the observed dependence on cation ordering is not a substrate or surface effect. For the Alloy film where the *A*-site cations are fully mixed (Figure 3a), the distortions observed in the Ni–O_{ap} bond lengths in the polar variants are strongly suppressed or absent. Thus, the Ni–O_{ap} distortions are correlated with polar ordering of the *A*-site cations within the RP f.u. We speculate that the reason for the Ni–O distortions being larger near the surface and smaller near the substrate for both polar variants may be due to a 'clamping' effect of the substrate.

The effect of cation ordering on the Ni–O_{eq} positions ("rumpling") is also visible, where the Ni is displaced away from the Ni-O equatorial plane. Figure 3d–f demonstrates the rumpling (quantified by the Z-height difference between the Ni and the O_{eq} plane) as a function of Z height inside each lattice u.c. for the three layering variants. 'Positive' rumpling indicates that the Ni displaces toward the surface more than the O_{eq} plane does. The Al-O_{eq} rumpling is also shown for the top four u.c. of each $LaSrAlO_4$ substrate for comparison. The overall trend is that LNS/LNS ordering creates 'negative' rumpling for some of the layers near the surface (by as much as 0.30 Å), while SNL/SNL ordering creates slightly "positive" rumpling in the same layers. The Alloy sample shows no clear trend in rumpling.

We have measured the magnetization of our samples with a SQUID magnetometer. These data did not show any evidence for long-range ferromagnetic order, though this does not rule out other forms of magnetic ordering. Our resistivity measurements show that the random alloy samples are metallic down to low temperatures. On the other hand, while the polar analogs have comparable resistivity at 300 K, they are weakly insulating at lower temperatures, with the resistivity increasing monotonically upon cooling. A detailed study of these properties is currently underway.

In order to understand the response of the LSNO structure to polar cation ordering, we carry out density functional calculations within the generalized gradient approximation (GGA) on the Alloy and LNS/LNS samples. We relax the full atomic

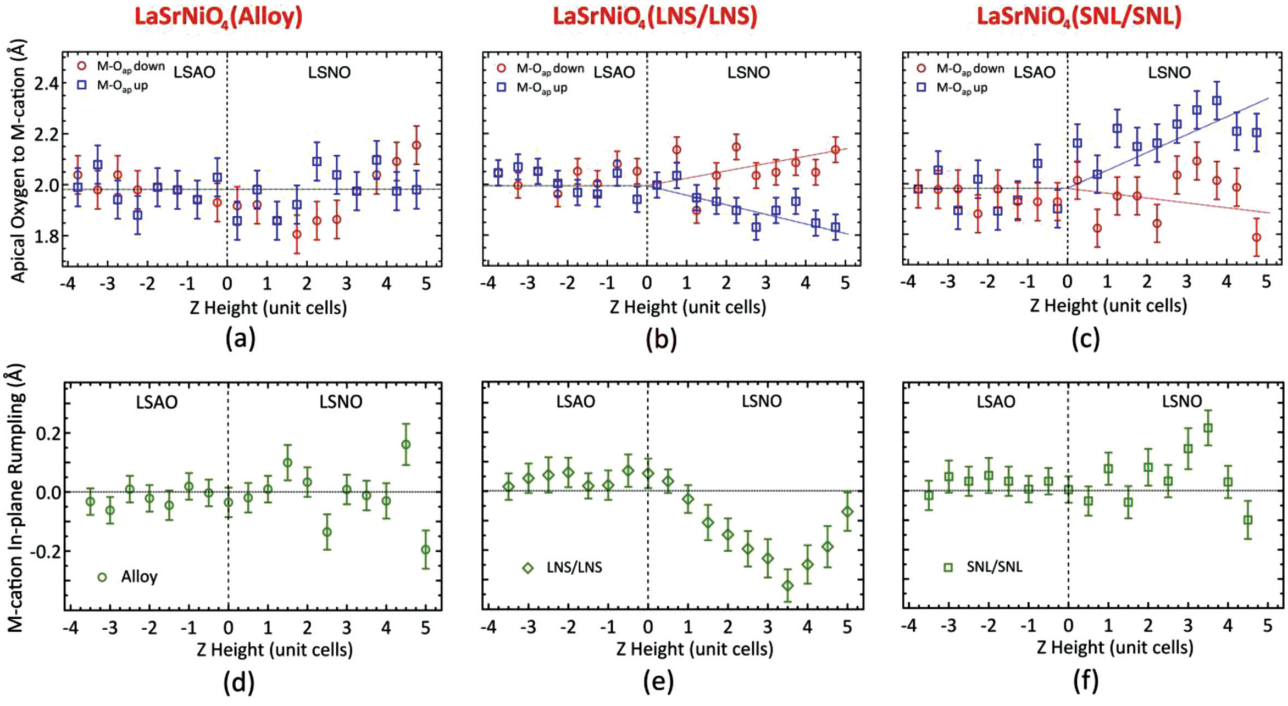

Figure 3. The evolution of the apical oxygen to *M*-site cation distance with the *A*-site cation distribution inside each lattice unit cell was shown for a) Alloy, b) LNS/LNS, and c) SNL/SNL. The vertical dotted line represents the nominal interface between substrate and the film. The Al-O_{ap} bond lengths are also shown for the top four unit cells of each $LaSrAlO_4$ substrate for comparison. The horizontal dashed line represents the bulk value of the apical oxygen to *M*-site cation distance. The straight lines in (b,c) are guides for the eye only. The evolution of *M*-cation in-plane atomic rumpling with the *A*-site cation distribution inside each lattice u.c. for d) Alloy, e) LNS/LNS, and f) SNL/SNL.

structure beginning with local atomic configurations generated from several symmetry-related crystal structures[15] under the constraints of the experimental lattice constants [Table S2, Supporting Information]. Consistent with the COBRA analysis, we find the introduction of $[LaO]^{(1+)}$ and neutral $[SrO]^{(0)}$ layers in the cation ordered LNS/LNS variant leads to distortions of the NiO_6 octahedral coordination, which reduce the polar *I4mm* symmetry (obtained solely from the La/Sr cation order in the RP structure) to *P4mm* with two crystallographically distinct Ni sites. Although we do not capture the long-range modulation in bonds lengths owing to the periodic boundary conditions of our simulations, we do find alternating long and short Ni–O_{ap} bonds along the *c*-axis, and rumpling [≈ <0.16 Å>, Supporting Information Table S2] of the Ni–O_{eq} plane—structural features both absent in the Alloy (Figure 2,3). These lattice distortions lead to acentric NiO_6 units, which we quantify by calculating molecular dipole moments in units of Debye (D) based on a point-charge model yielding 8.6 D, and 6.4 D, compared to 1.4 D for the polar ammonia molecule.[33]

In the polar variants, the asymmetric Ni-O bond environment should lead to additional O 2*p*– Ni 3*d* hybridization pathways not available to the Alloy configuration. A change in bond length causes a change in this hybridization and the effective electron count on the Ni. The change in the number of electrons localized to the Ni-site is referred to as "self-doping".[34] We probe the hybridized Ni states using polarized XAS near the Ni K-edge.[35] The X-rays are polarized along the *c*-axis (*c*-pol) and in the *a*–*b* plane (*ab*-pol) of the $LaSrNiO_4$ films. **Figure 4**a shows the comparison between the Alloy and LNS/LNS variants, each 16 u.c. thick. The main absorption edge is due to a nominal Ni 1*s*-4*p* dipole transition, where the final state is $4p_\sigma 3d^8\underline{L}$ for the *ab*-pol (referred to as $4p_\sigma$). The $\underline{L}$ symbol refers to a ligand hole on the coordinating oxygen atoms that arises as a result of strong hybridization with the Ni states, with electron transfer to the Ni 3*d* manifold. At lower energies, a weak pre-edge transition is also measured, as observed in other TMOs with octahedral coordinations,[36] and found to be stronger in *ab*-pol compared to *c*-pol XAS in all samples [Figure S4] consistent with the literature.[37] The central finding is that the *ab*-pol pre-edge feature is larger for the polar LNS/LNS sample compared to the random alloy, indicative of Ni oxidation and self-doping. Indeed, this is similar to trends observed in bulk $La_{2-x}Sr_xNiO_4$, where the larger *ab*-pol XAS pre-edge feature grows with hole doping (x) by more than a factor of 3 between $x = 0$ and $x = 1$, while for *c*-pol XAS the pre-edge feature remains relatively small.[35,37] In our samples, a similar effect

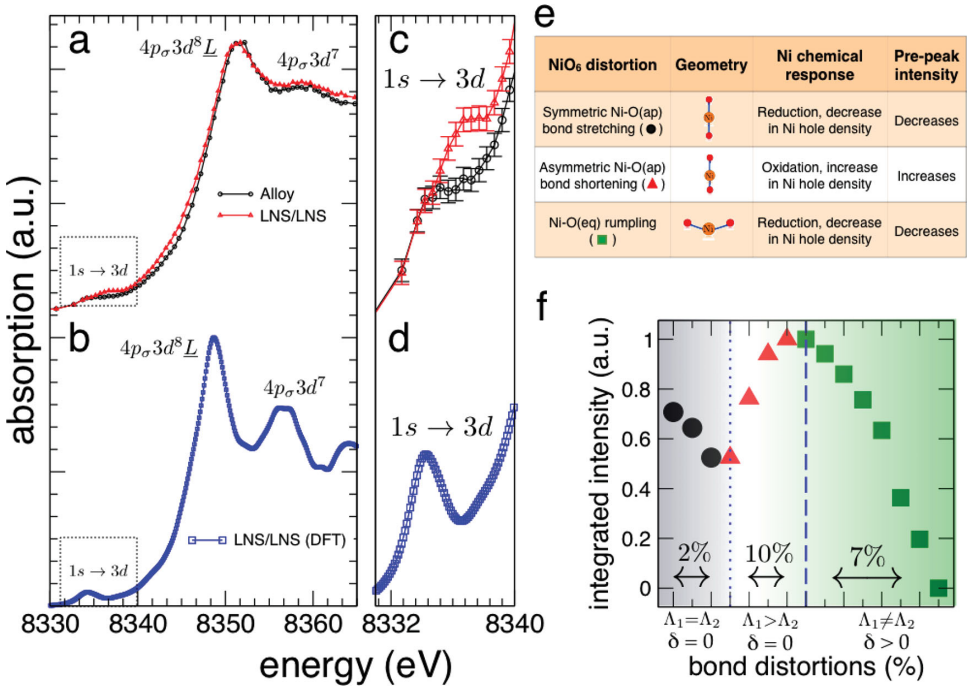

Figure 4. Electronic structure and electron-lattice effects in $LaSrNiO_4$. a) Experimental *ab*-pol X-ray absorption spectra near the Ni *K*-edge for Alloy (black, circle) and globally polar LNS/LNS variant (red, triangles) for films of identical thickness (16 u.c.). b) The total *ab*-pol absorption spectra (spin up + spin down) for the ground state LNS/LNS (blue, square) from DFT averaged over two Ni-sites. The main features (pre-edge and edges) in the *ab*-pol are labeled. The weak pre-edge feature in expanded view showing enhanced absorption for the c) experimental and d) DFT. The strong core-hole effect lowers the energy of the pre-edge feature in DFT. e) Summary table of the Ni–O bond distortions and its impact on the Ni chemistry. f) DFT calculated responses of three types of Ni-O bond distortions on the integrated intensity under the dipole pre-edge feature: symmetric Ni–$O_{(ap)}$ bond stretching (black, filled circles), asymmetric Ni–$O_{(ap)}$ bond shortening (red, filled triangles), and Ni–$O_{(eq)}$ rumpling (green, filled squares). Λ represents the Ni–$O_{(ap)}$ bond lengths (Λ_1 and Λ_2 being the long and short apical bonds respectively, in the center panel) and δ represents the rumpling distortions in the Ni–$O_{(eq)}$ plane. Our quantification scheme (% distortions) for Ni–$O_{(ap)}$ bonds uses the long Ni–$O_{(ap)}$ bond length (2.189Å) as the reference. On the other hand, rumpling distortions ($\delta > 0$) are quantified in terms of the deviation of the equatorial O–Ni–O bond angle from 180°. The maximum extent of each of the three distortions that we have simulated is labeled in the figure. We note that a 7% distortion in the O–Ni–O bond angle corresponds to a distortion of 0.20 Å in Figure 3 d–f.

is achieved without chemical substitution. We note that there is no measureable change in the pre-edge features for *c*-pol data [Figure S4, Supporting Information].

To isolate the structural distortions that produce the enhanced pre-edge peak in the XAS spectra, we calculated the Ni K-edge dipolar and quadrupolar components of the XAS spectra with a core-hole on the absorbing Ni-site for the LNS/LNS cation ordered variant (see Experimental Section). Our calculations capture the weak pre-edge feature with a more pronounced intensity for the *ab*-pol direction (Figure 4b) relative to the *c*-pol direction [Figure S5], as is observed in all measurements. Note that the quadrupolar contribution to the pre-peak is an order of magnitude smaller than the dipolar term (Figure S5, Supporting Information), and the intrasite mixing between Ni $3d_{x2\text{-}y2}$ and $4p_{x,y}$ orbitals in the LNS/LNS structure are symmetry-forbidden (see Experimental Section). Therefore, the pre-peak feature in the *ab*-pol spectra predominantly arises from the dipolar term (Ni 1*s* to hybridized 3*d*-2*p* state transition) and provides a signature for the hole doping effect.

We now discuss a computational experiment to identify the distortions responsible for the enhancement of the *ab*-pol pre-edge peak intensity of LNS/LNS variant relative to the Alloy by focusing on the pre-edge feature in the dipolar term of the *ab*-pol spectra. Since the ground state LNS/LNS structure exhibits two distinct distortions, asymmetrical Ni–O_{ap} bonds and rumpled Ni-O_{eq} planes, we isolate each contribution to the pre-edge peak by independently "freezing-in" each distortion pattern into the high symmetry *I*4*mm* phase with varying magnitude. Figure 4e depicts and summarizes the role of each distortion on the Ni state. The computed dipolar *ab*–pol spectra are discussed next.

First, we consider how symmetric bond stretching changes to the Ni-O_{ap} lengths alter the *ab*–pol feature by uniformly decreasing the length (Λ) in the absence of Ni-O_{eq} rumpling ($\delta = 0$). Although these distortions are directed at the O_{ap} atoms, they affect the crystal field splitting and modify the occupancies of both the in-plane ($d_{x2\text{-}y2}$) and out-of-plane (d_{z2}) frontier orbitals.[38] In our simulations, we probe the response of in-plane 3*d*-orbitals to the O_{ap} distortions. Figure 4f (left) shows that uniform stretching of the bond length from 2.138–2.189 Å leads to a decrease in the integrated area, thus a decrease in holes on Ni. Next, we apply an asymmetric bond compression to the Ni–O_{ap} bond lengths (Figure 4f, center), starting from the last symmetrical apical bond configuration where the average long Ni–O_{ap} bond matches that found in the calculated ground state and is close to that obtained from the experimental COBRA analysis. The asymmetric Ni-O_{ap} geometry (2.189 vs 1.954 Å) leads to a further enhancement in the pre-edge intensity (increase in Ni hole density) owing to the presence of a shorter Ni-O_{ap} bond. We now keep the apical bond geometry fixed at these lengths and introduce with increasing amplitude the Ni–O_{eq} rumpling. We find that as rumpling distortions increase [Figure 4f, right], the integrated intensity under the pre-edge peak rapidly decreases, indicating a reduction in Ni valence and an increase in oxygen ligand hole density [Figure 4f]. We summarize these results as follows: when the two Ni–O_{ap} bonds are long and symmetric, the oxygen ligand hole density is high. Shortening of these bonds leads to a transfer of holes to Ni (self-doping), which is further promoted by asymmetric Ni–O_{ap} bonds. In contrast, rumpling of the Ni-O_{eq} bonds, drives holes back to the oxygen site.

With this understanding, we attribute the enhanced *ab*-pol pre-edge feature in the LNS/LNS structure (compared to the Alloy) to the asymmetric Ni–O_{ap} bond environment, which is a direct result of the polar cation ordering. The shorter Ni–O_{ap} bond in the LNS/LNS variant compared to the longer (and symmetric) bonds in the Alloy allows the coordinating oxygen atoms to pull more electrons from the Ni cation. These distortions compete with and dominate over the effects of rumpling distortions in the LNS/LNS structure, which should reduce the observed pre-edge peak intensity. Thus, the Ni cations in LNS/LNS are more oxidized, with more holes, compared to the Alloy variant, despite possessing the same stoichiometry.

3. Conclusions

By manipulating the placement of the *A*-site dopant cations, we demonstrate a new structural design strategy that imposes large electrostatic bond strains in a single, chemically equivalent oxide material. In the presence of polar cation layering within the RP perovskite $LaSrNiO_4$, the oxygen atoms respond in a manner that remarkably alters both their physical and chemical bonding with Ni. This produces a change in the valence of the transition metal—without any change to the chemical doping—making it possible to access new regions of phase space in well-studied materials. This method can be extended to achieve greater bond strains in a broad spectrum of layered oxides containing cations of different valences. Even for *A*:*A*' compositions beyond 1:1, one can alter the local electrostatics of the *M*–O bonding through precise *A*-site cation placement in order to create local *M*–O bond strain.

Electrostatic bond strain within layered oxides may be used to tailor a host of important properties. These include higher superconducting T_c's in the cuprates by elongating the Cu–O_{ap} bonds,[5] where an increase in bond length of ≈10% could lead to a T_c enhancement of >40% in some materials.[39] In oxygen evolution reactions, superior catalytic activity was observed by modifying e_g orbital occupancies[40,41] and ligand hole densities.[42] Our approach may allow us to tailor these properties at the surfaces of transition metal oxides without explicit chemical doping. In the area of spintronics, the Rashba effect[43] is used to couple the electron spin and momentum via spin-orbit coupling. The effect, however, is typically limited to surfaces and interfaces where the effects of broken inversion symmetry are highest. We could use our approach to introduce asymmetric spin-orbit coupling by breaking inversion symmetry throughout the bulk of both normal[44] and ferromagnetic[45] conductors by creating ferroelectric-like polar distortions in metallic oxides.[46] This could lead to novel forms of spin-orbit torque and to the efficient generation and detection of pure spin currents. We may also be able to design faster ionic conductors in oxides by influencing interstitial site geometry via electrostatic bond strain.[47] Thus, employing electrostatics to engineer large local strains provides a fresh approach to control the properties of a wide range of oxide materials.

4. Experimental Section

Film Growth, Surface Structure, and Crystallinity: Epitaxial Ruddlesden-Popper (single layer) films of $LaSrNiO_4$ (LSNO) synthesized by oxide-MBE on isostructural (001)-oriented $LaSrAlO_4$ (LSAO) single crystal substrates ($a = b = 3.756$ Å, $c = 12.636$ Å) in pure ozone at a temperature of 550°C. Bulk LSNO has lattice parameters of $a = b = 3.826$ Å, $c = 12.45$ Å, and the epitaxial LSNO films exhibit a biaxial in-plane compressive strain of -1.8%. Films were grown to thicknesses of 5 u.c. (6.3 nm), 16 u.c. (20 nm), and 32 u.c. (40 nm). Further details of the film growth and structure, including *in-situ* reflective high energy electron diffraction, and ex situ atomic force microscopy, X-ray reflectivity, and X-ray diffraction can be found elsewhere.[16] Both in situ and ex situ structural probes, such as reflection high-energy electron diffraction, atomic force microscopy, X-ray reflectivity, and X-ray diffraction indicate that the films exhibit the K_2NiF_4 crystal structure and are atomically smooth with terraced surfaces, both during and after growth.[16]

Synchrotron Surface Diffraction Measurements and COherant Bragg Rod Analysis: The structural investigations were performed on a series of 5 full u.c. thick films for each LSNO structural variant at beamline 12-ID-D of the Advanced Photon Source (APS). The measurements were conducted on a six-circle Huber goniometer, using an X-ray energy of 16.5 KeV ($\lambda = 0.751419$ Å). The X-ray beam with a profile of 100 μm (vertical) × 500 μm (horizontal) had a flux of 2×10^{12} photons/sec. The angle of incidence is fixed at 1.2° to keep the X-ray footprint during non-specular scans. The 2D scattering images of various CTRs at each step in the reciprocal lattice unit were acquired by using a pixel array area detector (Dectris PILATUS 100 K). We measured the diffraction intensities along both specular and non-specular substrate-defined CTRs. The L-scan along each CTR was obtained by removing the background scattering contributions using the 2D images. The combined COBRA/Difference-Map algorithm was utilized to ensure rapid convergence. The reconstructed total structure factors were then Fourier transformed to obtain the 3D ED of the film and substrate with sub-Å resolution. [As seen in Figure S2, the final calculated and measured intensities along the CTRs are in good agreement.]

Density Functional Theory (DFT): DFT calculations were performed within the GGA[48] PBEsol[49] plus Hubbard-*U*[50] method as implemented in the plane wave code Quantum ESPRESSO using a 60 Ry planewave cut-off.[51] An effective Hubbard term of 3 eV was used to treat the correlated Ni-3*d* electrons, and ferromagnetic spin order was imposed. The core and valence electrons were treated with ultrasoft pseudopotentials.[52] The Brillouin-zone integrations were performed with a Methfessel-Paxton smearing[53] of 8 meV over an 8 × 8 × 5 Monkhorst-Pack[54] *k*-point mesh centered at Γ. In our self-consistent calculations, atomic positions were relaxed until the Hellmann-Feynman forces were <2 meV/Å and the total energy converged to 10^{-8} eV. Spin polarized Ni K-edge XAS calculations were performed with and without core-hole corrections [Figure S5] using a $\sqrt{2} \times \sqrt{2} \times 1$ supercell on the LNS/LNS ground state structure by means of the XSpectra package[55] that employs the GIPAW reconstruction[56] of the all-electron wavefunction. We used a 4 × 4 × 2 *k*-mesh sampling, 1 eV linewidth, and Lanczos calculations converged to a tolerance of 0.1 meV. Two sets of coordinates of the incident X-ray polarization vector were chosen: *ab*-pol and *c*-pol to replicate the experimental setup. The necessary symmetry-allowed condition for an electric dipole transition in the *ab*-pol direction of a 1*s* electron to a *d* orbital of Ni^{3+} cation is the existence of a common irreducible representation to which both the d_{x2-y2} and $p_{x,y}$ orbitals would belong. If a point group satisfies this condition, then the electric dipole transition of a 1*s* electron occurs to a *p-d* hybridized orbitals, accompanied by a quadrupolar transition to *d* orbitals (i.e., enhancement in the pre-peak feature).[57] However, our symmetry analysis using character tables appropriate for each structural variant reveals that in both Alloy and LNS/LNS sample, the intrasite mixing between $p_{x,y}$ and d_{x2-y2} orbitals are symmetry-forbidden. As a result, the pre-peak feature in the *ab*-pol spectra arises predominantly from the hybridization between Ni 3*d* and O 2*p* states.

Polarized X-Ray Absorption Near-Edge Spectroscopy: Measurements were carried out at Beamline 4-ID-D of the APS. Grazing incidence geometry was used whereby the angle between the focused X-ray beam and the sample surface was 0.6° in order to increase the interacting sample volume (absorption length >> sample thickness). The sample was rotated around the incident X-ray beam so that the electric field of the X-rays was either in the plane of the sample (*ab*-pol) or (nearly) perpendicular to it (*c*-pol). XAS was measured in fluorescence geometry by detecting the changes in Ni Kα emission with a four-element Si drift diode detector as the incident energy is scanned across the Ni K-edge. A total of six samples were measured, using X-rays polarized along the *c*-axis (*c*-pol) and in the *a–b* plane (*ab*-pol) of $LaSrNiO_4$.

Supporting Information

Supporting Information is available from the Wiley Online Library or from the author.

Acknowledgements

Work at Argonne National Laboratory, including use of facilities at the Center for Nanoscale Materials and the Advanced Photon Source, was supported by the U.S. Department of Energy, Office of Basic Energy Sciences under contract No. DE-AC02–06CH11357. The authors would like to acknowledge Antonio Cammarata for assisting with the DFT calculations and Michel van Veenendahl for discussions. P.V.B. and J.M.R. were supported by DARPA (grant no. N66001–12–4224) and ARO (W911NF-12–1–0133), respectively. DFT calculations were performed using the Garnet and Spirit DOD facilities supported by the HPCMP. B.N-C, J.H., and A.B. were supported by the Department of Energy, Office of Basic Energy Sciences, Materials Science and Engineering Division.

Received: April 4, 2014
Revised: July 15, 2014
Published online: September 5, 2014

[1] S. Maekawa, "*Physics of Transition Metal Oxides*", Ch. 1, (Eds: S. Maekawa, T. Tohyama, S. E. Barnes, S. Ishihara, W. Koshibae, G. Khaliullin), Springer, Berlin **2004**.
[2] E. Dagotto, *Nanoscale phase separation and colossal magnetoresistance: The Physics of Manganites and Related Compounds*, Springer, Berlin **2003**.
[3] Y. Ohta, T. Tohyama, S. Maekawa, *Phys. Rev. B* **1991**, *43*, 2968.
[4] N. A. Hill, *J. Phys. Chem. B* **2000**, *104*, 6694.
[5] H. Eisaki, N. Kaneko, D. L. Feng, A. Damascelli, P. K. Mang, K. M. Shen, Z.-X. Shen, M. Greven, *Phys. Rev. B* **2004**, *69*, 064512.
[6] J. H. Haeni, P. Irvin, W. Chang, R. Uecker, P. Reiche, Y. L. Li, S. Choudhury, W. Tian, M. E. Hawley, B. Craigo, A. K. Tagantsev, X. Q. Pan, S. K. Streiffer, L. Q. Chen, S. W. Kirchoefer, J. Levy, D. G. Schlom, *Nature* **2004**, *430*, 758–761.
[7] Y. Konishi, Z. Fang, M. Izumi, T. Manako, M. Kasai, H. Kuwahara, Y. Tokura, *J. Phys. Soc. Jpn.* **1999**, *68*, 3790–3793.
[8] J. H. Lee, L. Fang, E. Vlahos, X. Ke, Y. W. Jung, L. F. Kourkoutis, J.-W. Kim, P. J. Ryan, T. Heeg, M. Roeckerath, V. Goian, M. Bernhagen, R. Uecker, P. Chris Hammel, K. M. Rabe, S. Kamba, J. Schubert, J. W. Freeland, D. A. Muller, C. J. Fennie, P. Schiffer, V. Gopalan, E. Johnston-Halperin, D. G. Schlom, *Nature* **2010**, *466*, 954–958.
[9] H. Chen, D. P. Kumah, A. S. Disa, F. J. Walker, C. H. Ahn, S. Ismail-Beigi, *Phys. Rev. Lett.* **2013**, *110*, 186402.
[10] H. Zhou, Y. Yacoby, V. Y. Butko, G. Logvenov, I. Božović, R. Pindak, *Proc. Natl. Acad. Sci. U.S.A.* **2010**, *107*, 8103–8108.

[11] A. Gozar, G. Logvenov, L. F. Kourkoutis, A. T. Bollinger, L. A. Giannuzzi, D. A. Muller, I. Bozovic, *Nature* **2008**, *455*, 782–785.
[12] J. P. Attfield, A. L. Kharlanov, J. A. McAllister, *Nature* **1998**, *394*, 157.
[13] A. Warshel, M. Levitt, *J. Mol. Biol.* **1976**, *103*, 227–249.
[14] Y. Yacoby, M. Sowwan, E. Stern, J. O. Cross, D. Brewe, R. Pindak, J. Pitney, E. M. Dufresne, R. Clarke, *Nat. Mater.* **2002**, *1*, 99–101.
[15] P. V. Balachandran, D. Puggioni, J. M. Rondinelli, *Inorg. Chem.* **2013**, *53*, 336.
[16] B. B. Nelson-Cheeseman, H. Zhou, J. D. Hoffman, P. V. Balachandran, J. M. Rondinelli, A. Bhattacharya, unpublished.
[17] B. B. Nelson-Cheeseman, A. B. Shah, T. S. Santos, S. D. Bader, J.-M. Zuo, A. Bhattacharya, *Appl. Phys. Lett.* **2011**, *98*, 072505.
[18] L. Yan, H. J. Niu, G. V. Duong, M. R. Suchomel, J. Bacsa, P. R. Chalker, J. Hadermann, G. van Tendeloo, M. J. Rosseinsky, *Chem. Sci.* **2011**, *2*, 261–272.
[19] P. K. Davies, *Curr. Opin. Solid State Mater. Sci.* **1999**, *4*, 467–471.
[20] F. Millange, V. Caignaert, B. Domengès, B. Raveau, *Chem. Mater.* **1998**, *10*, 1974.
[21] A. Ohtomo, D. A. Muller, J. L. Grazul, H. Y. Hwang, *Nature* **2002**, *419*, 378.
[22] P. A. Salvador, A.-M. Haghiri-Gosnet, B. Mercey, M. Hervieu, B. Raveau , *Appl. Phys. Lett.* **1999**, *75*, 2638.
[23] A. Bhattacharya, S. J. May, S. G. E. te Velthuis, M. Warusawithana, X. Zhai, B. Jiang, J.-M. Zuo, M. R. Fitzsimmons, S. D. Bader, J. N. Eckstein ,*Phys. Rev. Lett.* **2008**, *100*, 257203.
[24] H. Yamada, M. Kawasaki, Y. Ogawa, Y. Tokura, *Appl. Phys. Lett.* **2002**, *81*, 4793.
[25] M. P. Warusawithana, E. V. Colla, J. N. Eckstein, M. B. Weissman, *Phys. Rev. Lett.* **2003**, *90*, 036802.
[26] H. N. Lee, H. M. Christen, M. F. Chisholm, C. M. Rouleau, D. H. Lowndes, *Nature* **2005**, *433*, 395–399.
[27] S. J. May, P. J. Ryan, J. L. Roberston, J.-W. Kim, T. S. Santos, E. Karapetrova, J. L. Zarestky, X. Zhai, S. G. E. te Velthuis, J. N. Eckstein, S. D. Bader, A. Bhattacharya, *Nat. Mater.* **2009**, *8*, 892.
[28] C. N. R. Rao, B. Raveau, *Transition Metal Oxides,* VCH, New York **1995**.
[29] D. D. Fong, C. Cionca, Y. Yacoby, G. B. Stephenson, J. A. Eastman, P. H. Fuoss, S. K. Streiffer, C. Thompson, R. Clarke, R. Pindak, E. A. Stern, *Phys. Rev. B* **2005**, *71*, 144112.
[30] The atomic number Z for Sr is 38. However, we use $Z = 35$ here due to the fact that the X-ray measurements were performed at an energy near the K-edge of Sr, where the effective Z is about 3 electrons less.
[31] Y. Yacoby, H. Zhou, R. Pindak, I. Božović, *Phys. Rev. B* **2013**, *87*, 014108.
[32] In our films, this may be due to 'archipelagos' near terrace edges, where islands of single formula-unit height are observed with atomic force microscopy. This could contribute towards reduction in the integrated electron number for the last layer.
[33] *CRC handbook of Chemistry and Physics,* (Ed: W. M. Haynes), 94th edn, CRC press, Boca Raton **2014**.
[34] M. A. Korotin, V. I. Anisimov, D. I. Khomskii, G. A. Sawatzky, *Phys. Rev. Lett.* **1998**, *80*, 4305.
[35] A. Sahiner, M. Croft, S. Guha, I. Perez, Z. Zhang, M. Greenblatt, P. A. Metcalf, H. Jahns, G. Liang, *Phys. Rev. B* **1995**, *51*, 5879.
[36] F. de Groot, G. Vanko, P. Glatzel, *J. Phys.: Condens. Matter* **2009**, *21*, 104207.
[37] A. Sahiner, M. Croft, Z. Zhang, M. Greenblatt, I. Perez, P. Metcalf, H. Jhans, G. Liang, Y. Jeon, *Phys. Rev. B* **1996**, *53*, 9745.
[38] H. Tolentino, M. Medarde, A. Fontaine, F. Baudelet, E. Dartyge, D. Guay, G. Tourillon, *Phys. Rev. B* **1992**, *45*, 8091.
[39] Y. Ohta, T. Tohyama, S. Maekawa, *Phys. Rev. B* **1991**, *43*, 2968.
[40] J. Suntivich, H. A. Gasteiger, N. Yabuuchi, H. Nakanishi, J. B. Goodenough, Y. Shao-Horn, *Nat. Chem.* **2011**, *3*, 546–550.
[41] J. Suntivich, K. J. May, J. B. Goodenough, H. A. Gasteiger, Y. A. Shao-Horn, *Science* **2011**, *334*, 1383–1385.
[42] J. Suntivich, W. T. Hong, Y.-L. Lee, J. M. Rondinelli, J. B. Goodenough, B. Dabrowski, J. W. Freeland, Y. Shao-Horn, *J. Phys. Chem. C* **2014**, *118*, 1856–1863.
[43] Y. A. Bychkov, E. I. Rashba, *J. Phys. C: Solid State Phys.* **1984**, *17*, 6039.
[44] T. Koga, N. Junsaku, A. Tatsushi, T. Hideaki, *Phys. Rev. Lett.* **2002**, *89*, 046801.
[45] I. M. Miron, G. Gaudin, S. Auffret, B. Rodmacq, A. Schuhl, S. Pizzini, J. Vogel, P. Gambardella, *Nat. Mater.* **2010**, *9*, 230–234.
[46] Y. Shi, Y. Guo, X. Wang, A. J. Princep, D. Khalyavin, P. Manuel, Y. Michiue, A. Sato, K. Tsuda, S. Yu, M. Arai, Y. Shirako, M. Akaogi, N. Wang, K. Yamaura, A. T. Boothroyd, *Nat. Mater.* **2013**, *12*, 1024–1027.
[47] B. Yildiz, *MRS Bull.* **2014**, *39*, 147.
[48] J. P. Perdew, K. Burke, M. Ernzerhof, *Phys. Rev. Lett.* **1996**, *77*, 3865.
[49] J. P. Perdew, A. Ruzsinszky, G. I. Csonka, O. A. Vydrov, G. E. Scuseria, L. A. Constantin, X. Zhou, K. Burke, *Phys. Rev. Lett.* **2008**, *100*, 136406.
[50] S. L. Dudarev, G. A. Botton, S. Y. Savrasov, C. J. Humphreys, A. P. Sutton, *Phys. Rev. B* **1998**, *57*, 1505.
[51] P. Giannozzi, S. Baroni, N. Bonini, M. Calandra, R. Car, C. Cavazzoni, D. Ceresoli, G. L. Chiarotti, M. Cococcioni, I. Dabo, A. Dal Corso, S. de Gironcoli, S. Fabris, G. Fratesi, R. Gebauer, U. Gerstmann, C. Gougoussis, A. Kokalj, M. Lazzeri, L. Martin-Samos, N. Marzari, F. Mauri, R. Mazzarello, S. Paolini, A. Pasquarello, L. Paulatto, C. Sbraccia, S. Scandolo, G. Sclauzero, A. P. Seitsonen, A. Smogunov, P. Umari, R. M. Wentzcovitch, *J. Phys.: Condens. Matter* **2009**, *21*, 395502.
[52] D. Vanderbilt, *Phys. Rev. B* **1990**, *41*, 7892.
[53] M. Methfessel, A. T. Paxton, *Phys. Rev. B* **1989**, *40*, 3616.
[54] H. J. Monkhorst, J. D. Pack, *Phys. Rev. B* **1976**, *13*, 5188.
[55] C. Gougoussis, M. Calandra, A. Seitsonen, F. Mauri, *Phys. Rev. B* **2009**, *79*, 045118.
[56] C. J. Pickard, F. Mauri, *Phys. Rev. B* **2001**, *63*, 245101.
[57] T. Yamamoto, *X-Ray Spectrom.* **2008**, *37*, 572–584.